Research Article Vol. 13, No. 5 / 1 May 2023 / Optical Materials Express 1228

Optical Materials EXPRESS

Out of focus ultrafast processing of metals for reduced secondary electron yield

ROBIN UREN,[1,*] A. DIN,[1] S. WACKEROW,[1] E. BEZ,[2] S. PFEIFFER,[2] M. RIMOLDI,[2] M. HIMMERLICH,[2] M. TABORELLI,[2] AND A. ABDOLVAND[1]

[1] *Materials Science & Engineering Research Cluster, School of Science & Engineering, University of Dundee, Dundee, DD1 4HN, United Kingdom*
[2] *European Organization for Nuclear Research, CERN, Geneva, Switzerland*
[*] *ruren001@dundee.ac.uk*

Abstract: We have demonstrated out-of-focus ultrafast pulsed laser processing of copper with a variable working distance, without the need for mechanical movement. This was achieved by employing a diffractive optical element. The method has been demonstrated in a practical application to reduce the secondary electron yield (SEY) of copper to below 1.3. We show that using an extended focus element not only increases the consistency of processing across a range of working distances, but also changes the topography of the produced structures, reducing the SEY. This presented approach shows promise in facilitating the Large Hadron Collider's (LHC's) upcoming high luminosity upgrade by preventing electron clouds.

Published by Optica Publishing Group under the terms of the Creative Commons Attribution 4.0 License. Further distribution of this work must maintain attribution to the author(s) and the published article's title, journal citation, and DOI.

1. Introduction

A distinct advantage of laser processing is the ability to produce more intricate shapes with smaller feature sizes compared to conventional mechanical machining. As the technology has matured more demanding applications have arisen including the need to machine with a variable working distance. Standard solutions to this involve moving either the sample, which may not always be possible, or moving the focusing lens, which is often challenging mechanically to maintain the lateral beam position [1–3]. Both can also limit processing speeds. Another solution is to increase the focal spot size of the beam and thereby increase the Rayleigh length. However, this reduces the focal intensity and increases the minimum feature size making it unsuitable for some applications. This is of particular concern with ultrafast processing due to the high peak powers needed to reach the multiphoton absorption required for ablation [4].

Diffractive optical elements (DOEs) as a technology have been developing since the discovery of diffraction [5]. Diffractive optics have long found applications where refractive and reflective optics are not suitable. Typical applications include X-ray and extreme UV imaging [6–8], converting gaussian beams to non-gaussian profiles [9–11] and as non-polarising beamsplitters [12–14]. Other advantages of DOEs include typically leaving the beam size, divergence and polarisation unchanged as well as being comparatively thin and lightweight. These advantages of versatility come with downsides such as power losses due to limited diffraction efficiency and a high degree of wavelength sensitivity.

One subset of DOEs extends the depth of focus of a laser beam beyond the Rayleigh length of a gaussian beam. This is achieved by modifying a typical phase only zone plate [15] (or its amplitude equivalent) so that the focal distance has an angular variation, known as a 'petal' DOE, or by merging it with the phase delay caused by an axicon, called an axilens DOE [16–18]. The former causes different parts of the beam to be focussed at different distances while the latter achieves a similar effect through partial conversion to a Bessel beam. These have been

#484235 https://doi.org/10.1364/OME.484235
Journal © 2023 Received 1 Feb 2023; revised 24 Mar 2023; accepted 24 Mar 2023; published 10 Apr 2023

Optical Materials EXPRESS

applied extensively in microscopy and imaging [19–23]. Here, we propose the application of focal extension DOEs for ultra-fast laser surface structuring.

In our previous work we have processed the surface of copper with nanosecond and picosecond, 532 nm laser pulses in order to reduce the material's secondary electron yield (SEY) [24–28]. The SEY of a material is a measure of the number of secondary electrons emitted from a surface when impacted by a primary electron of a given energy. Strong electron emissivity can be beneficial in some applications, i.e. it is the mechanism by which scanning electron microscope (SEM) images are obtained and photo-multiplier tubes amplify a signal [29]. It is detrimental, however, in space science, high power microwave and plasma devices, and particle accelerators where the excessive electron emission can lead to surface charging, electron cloud formation and damage from multipactor events [30–33]. Previously, we have shown a reduction in the SEY of copper by creating laser engineered surface structures (LESS) via inscribing trenches into the surface and covering it with a nanostructure made of re-deposited copper and copper oxide particles. This significantly increases the chance that a given secondary electron will be re-absorbed by the surface after emission. This effect has been explored in detail through both experiment and numerical modelling [34–39]. Simulations indicate that the aspect ratio of the trench is particularly key, with higher ratios of depth to width creating better trapping for electrons.

CERN is about to undertake the High Luminosity upgrade to the LHC for 2026 [40,41]. This greater luminosity means surfaces within the collider will be bombarded with a larger number of electrons. Within the surfaces that enclose the proton beam these processes cause problems by generating electron clouds that induce beam instabilities and cause heat transfer to the cryogenic plant used to cool the superconducting magnets [42]. This is of particular issue for the copper beam screens which have an initial SEY of 2.0-2.4 [37], depending on surface contamination. Their SEY can be further reduced through the practice of beam scrubbing, however the SEY still typically remains above one [43]. This copper takes the form of a thin, on average 75 μm, layer on the inner surface of the tube, which has a hippodrome cross section [42]. We have previously demonstrated a reduction in the SEY of flat copper surfaces by pulsed laser processing trenches into the surface [25,27,44]. We are also developing a combined fibre and robot system to process the inner beam screen surfaces in situ. The hippodrome shape presents a significant challenge as the distance from the centre of the tube, where the laser source will emanate from, has a variable distance from the tube walls. This varies the working distance of the laser by approximately 5 mm, requiring a system that can process consistently 2.5 mm either side of the laser focus. As the internal cross section of the beam screen is less than 50 mm, it is technically challenging to mechanically move the focusing lens within the robot, and it is not possible to move the beam screen. Increasing the focal spot size will widen the trenches, reducing the aspect ratio and limiting SEY reduction. A novel solution is therefore required. Here, we demonstrate that using an extended focus DOE not only fulfills the requirements of the process, but changes the topography of the trenches, further reducing the SEY.

2. Optics of axilens diffractive optical elements

For these experiments a commercially available EF-014-1030 axilens DOE from HOLO/OR was used. This has an 11 mm diameter, 3 mm thickness, is anti-reflection (AR) coated on both surfaces for 1030 nm light, and has minimal diffraction losses. Testing showed that there was no observable optical loss when measured on a typical thermal power meter. The polarisation of the laser was also unaffected. The DOE does not focus the light and is designed to be paired with a conventional focusing lens to allow for greater flexibility. All tests were conducted with a Light Conversion Carbide laser operating at 1030 nm wavelength and a 400 kHz repetition rate. A collimated beam with a 2.0 mm radius was centred on the DOE with the focusing lens placed immediately behind.

For best comparison with our previous work we initially used a 150 mm focal length lens producing a 31 μm radius focal spot. Throughout this paper all beam radii, unless otherwise stated, are measured according to the second moment of intensity standard [45]. For gaussian beams this corresponds with the point at which the power drops to $1/e^2$ of the maximum intensity. We measured the beam radius through the focus using a Spiricon SP620U CCD camera. Looking at Fig. 1, we can see the DOE creates two distinct foci. One approximately 4mm before the focal plane of the lens and the second 4mm behind it. These foci have a larger beam radius of 54 μm than that with the lens only. Between the foci the beam radius increases to an average, almost flat, beam radius of 59 μm. The beam waist is defined as the point of a planar wavefront [46], which for a gaussian beam is also the point of minimum radius. For the DOE modified beam, the planar wavefront occurs in the middle of the flat section, at the focal point of the lens, but not at the points of minimum radius. This is important for defining the Rayleigh range of the DOE beam as being referenced on the beam radius at the planar wavefront. This definition gives a Rayleigh range of 7.9 mm, compared to the 2.9 mm of the lens only beam. The average beam radius within the Rayleigh range is 59.9 μm with the DOE but is 38.3 μm without it. As the DOE is increasing the radius of the beam through the focus, it will not perform in a directly comparable way in machining applications.

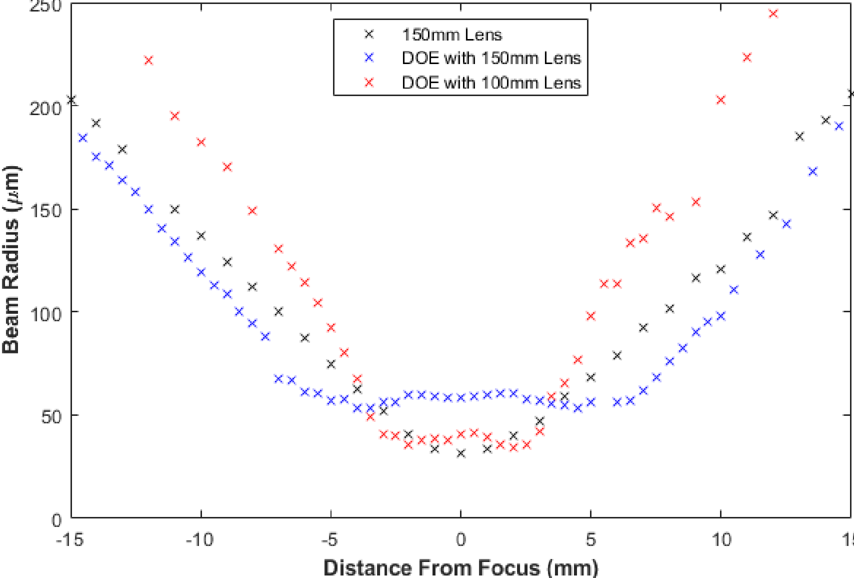

Fig. 1. Beam radius of a 2 mm radius collimated beam focused through a 150 mm spherical lens, a 150 mm lens with an axilens DOE and a 100 mm lens with an axilens DOE.

To achieve the same minimum focal spot size we exchanged the lens for one with a 100 mm focal length. Combined with the DOE this produced a minimum focal spot radii of 35 μm positioned 2 mm either side of the focal plane. This gives an average beam radius through the Rayleigh range of 39.7 μm and a Rayleigh range of 3.6 mm. Outside this range the beam diverges more quickly. Radii comparisons are summarised in Table 1. The DOE therefore reduces the average spot size through a given distance from the focal plane, whilst simultaneously extending the Rayleigh range of the beam for a target focal spot size. For the remainder of this paper the beam profile generated by the DOE and 100 mm lens will be referred to as 'the DOE beam'.

Looking at the beam profile, the beam has been transformed into a series of concentric rings. As this is focused, it coalesces into two rings, the inner of which collapses into a gaussian like

Optical Materials EXPRESS

Table 1. Summation of beam radii and Rayleigh ranges for the beams presented in Fig. 1.

	Minimum Radius μm	Beam Waist μm	Rayleigh Range mm	Average Radius Through Rayleigh Range μm
150 mm Lens	31.4	31.4	2.9	38.3
DOE and 150 mm Lens	53.7	58.6	7.9	59.9
DOE and 100 mm Lens	34.9	40.7	3.6	39.7

central peak with a significant shoulder, Fig. 2(a). A key difference between this and a beam focussed without the DOE is that not all the power is concentrated in this central region as a significant amount is in the outer rings and this continues throughout the focal region. This is more clearly seen in the log scale images in Fig. 3. This can be considered the beginning of the focal region and is approximately 4 mm before the true focus. The central region then further collapses to a true gaussian, Fig. 2(b). This represents the point with minimum beam radius. The innermost outer ring then collapses into the central peak and they create a disc-shaped central intensity spot with a lower peak power, c. At the true focus the beam has a clean, ring shaped intensity, still surrounded by further concentric rings, d. This process then reverses the other side of the focus, e. The beam then returns to the series of concentric rings outside the focal region, f. Figure 2(g) and (h) show x-z composite images of the DOE and a comparable theoretical gaussian beam to that depicted in Fig. 1 as they go through a focus. This clearly shows the extension of the high intensity region by the DOE and the twin foci either side of the ring focus.

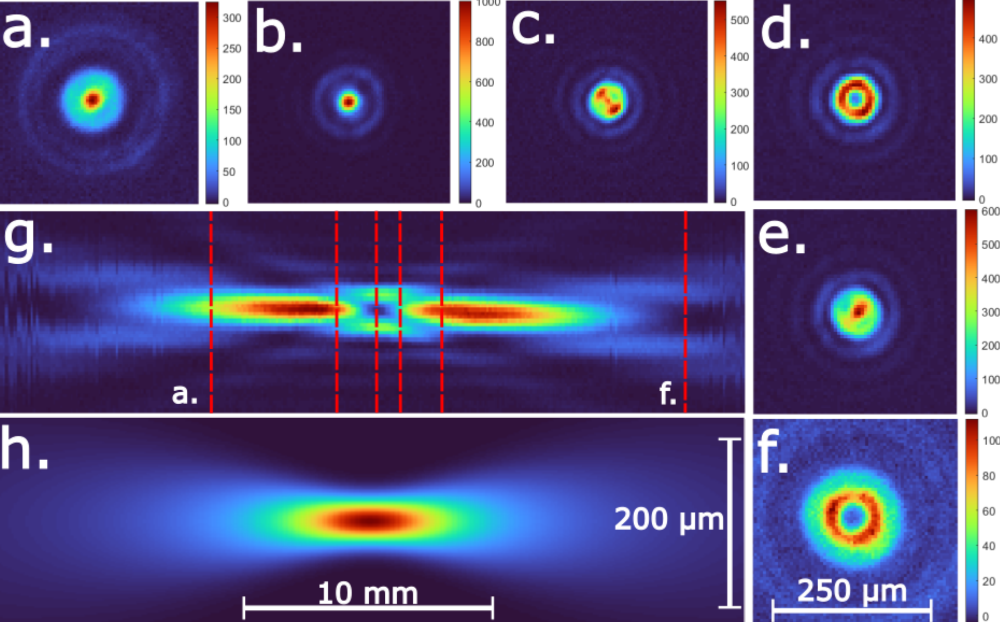

Fig. 2. a.-f. Selected images of the axilens DOE beam, orthogonal to the optical axis as it propagates through the focus. The colour scale is normalised in each image to best show the beam shape but colour bars can be used for comparison. Their position in the focus is indicated in image g. by the vertical dashed lines with the leftmost being a. running through to the rightmost being f. Image g. is a composite of 300 1D cross sections through the beam centre of the DOE beam focussed by the 100 mm lens. h. is an equivalent composite image of a theoretical gaussian beam focussed by a 150 mm lens as shown in Fig. 1.

Optical Materials EXPRESS

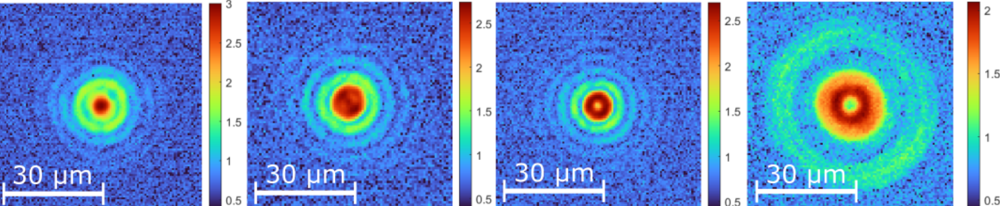

Fig. 3. Log scale versions of the images shown in Fig. 2 (b.-d.) and (f.). The images colour scales are normalised in each image to best show the outer power rings.

We can see measuring the beam diameter as defined by the second moment of intensity does not fully capture the behaviour of a beam modified by the axilens DOE. We therefore define a metric to better illustrate the beam's behavior that we will call the fractional power density (FPD), ρ_P, defined in Eq. (1). Here, I is the local intensity of the beam, r the radius as measured from the beam centre, θ the azimuthal angle, and z the displacement from the focal plane. Simply this is the percentage of the power concentrated within a given radius of the beam.

$$\rho_P(z) = \frac{\int_0^r \int_0^{2\pi} I(z, r, \theta)\mathrm{d}r\mathrm{d}\theta}{\int_0^\infty \int_0^{2\pi} I(z, r, \theta)\mathrm{d}r\mathrm{d}\theta} \quad (1)$$

If we set r in this equation to be equal to the second moment of intensity beam radius at each value of z, so its value as fluctuates with z, we find an ideal gaussian beam has constant $\rho_P(z)$ at all points. This is not true for the beam modified by the DOE, where the relative FPD varies significantly, see the solid red line in Fig. 4. Outside the key focal region it is lower than that of a gaussian beam (dashed red line), at 78% as compared to 86.5%. Within the focal region this increases to fluctuate between 80% and 88% peaking at the focal plane with the ring shaped beam. This shows that the relative FPD is also fluctuating as well as the beam radius, though not synchronously.

It is also possible that only the higher intensities located more to the centre of the beam will be relevant to machining applications. Looking at the relative FPD when r is set equal to the point at which $I(z, r, \theta)$ is equal to 50% of its maximum for a given z, effectively half the FWHM, we see a much more dramatic variation in the DOE beam, see the solid blue line in Fig. 4(b). A pure gaussian beam will have 50% of its total power within this region (blue dashed line). For the DOE this relative FPD fluctuates around this value outside the focal region. It then varies rapidly through the focal region from a minimum of 15% either side of the point of minimum focus up to 70% through the ring shaped region. This variation in FPD is largely opposing the variation in beam radius, which is also more significant with this tighter definition of beam radius, see the solid black line. This smooths out the intensity and improves consistency through the focus. The FPD is however, on average lower than that of a gaussian beam, perhaps necessitating more average power to match the intensity impacting the machining surface.

Another insightful measurement is to determine the fixed FPD. Defined by setting r in Eq. (1) to a fixed value through the focus, rather than one dependant on z. For an example we use the average beam radius of the gaussian beam through the focal region, i.e. 38.3 μm. Figure 4(c) compares the DOE modified beam to that of a pure, theoretical gaussian. We can see that while the gaussian has a higher fixed FPD in the actual focus of the beam by 7%, as we move 1.7 mm either side of the focus the fixed FPD is equal for both beams and beyond this the DOE beam's fixed FPD is higher. The DOE beam drops off more quickly at 3.5 mm away from the focus and again having lower fixed FPD by 4.2 mm away from the focus. We also see that the fixed FPD is much flatter through the focal region. This assists with maintaining the performance of the beam across a larger range of working distances.

Optical Materials EXPRESS

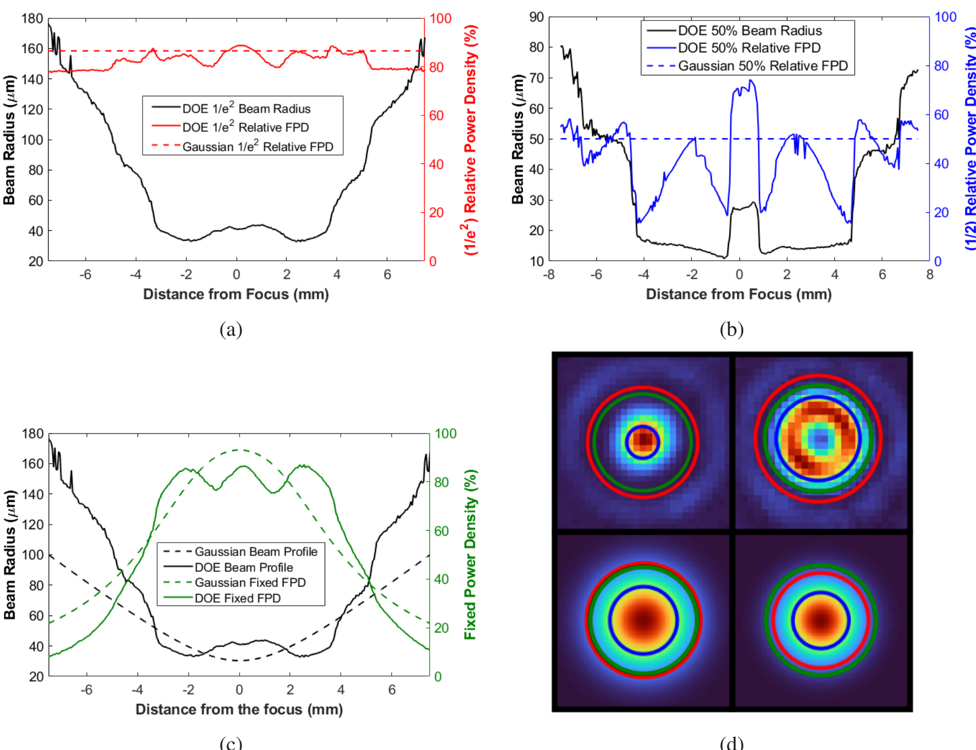

Fig. 4. (a.) Comparison between the relative FPD contained within the $1/e^2$ beam radius of a gaussian (dashed red line) and DOE (solid red line) beam through the focus. The DOE beam profile is depicted as the solid black line. (b.) the same comparison but within a radius defined by the point at which the power drops to 50% of its maximum power. The 50% radius profile of the DOE beam is depicted in black. (c). The fixed fractional power density within a 38.3 μm radius for the DOE (solid green line) and gaussian (dashed green line) beam. (d.) Images of the DOE (top row) and gaussian (bottom row) beam at the focal plane (right column) and 2mm before the focus (left column). The red ring indicates the $1/e^2$ radius, the blue the 50% radius and the green the 38.3 μm radius.

3. Implementing a DOE for reducing SEY

To perform the laser processing experiments we used pulse lengths between 300 fs and 10 ps. Copper samples are mounted onto two Aerotech PRO115SL linear stages to allow for x/y motion. The beam is directed onto a third, vertically mounted, Aerotech MPS75SL, linear stage. Upon this is mounted the focusing lens, DOE and a gas nozzle delivering nitrogen at 5.8 l/min. The stages are synchronised with the shutter control of the laser, allowing us to precisely control the focal position of the laser in three dimensions. The nitrogen reduces oxidation [28] and helps remove debris from the processing area along with vacuum extraction.

Initially the damage threshold of blank copper samples was measured, without the DOE, using the method outlined by Kirkwood *et. al.* [47]. We measured at three different pulse lengths and four different numbers of pulses per spot, adjusted using a pulse picker, in order to optimise the machining parameters. The focal spot size was measured by applying the second moment of intensity method to CCD images of the focal spot. The damage spots were measured using a Keyence VHX-1000 digital microscope. Table 2. outlines the results.

Optical Materials EXPRESS

Table 2. Damage thresholds of copper at various pulse lengths using a 1030 nm wavelength and 400 kHz repetition rate laser.

Damage Threshold (J/cm^2)	N = 1	N = 10	N = 100	N = 1000
10 ps	1.56 ± 0.15	1.04 ± 0.25	0.28 ± 0.14	0.48 ± 0.13
800 fs	0.90 ± 0.13	0.73 ± 0.09	0.36 ± 0.08	0.32 ± 0.12
300 fs	0.82 ± 0.08	0.73 ± 0.13	0.36 ± 0.08	0.28 ± 0.11

The single pulse damage threshold is significantly higher at 1030 nm at all pulse lengths compared to our previous measurement at 532 nm of 0.24 Jcm^{-2} [27] due to the higher reflectivity of copper at 1030 nm. However, there is a significant damage incubation effect, likely caused by heat accumulation, at all pulse lengths. This drops the damage threshold to approximately 0.3 Jcm^{-2}. We believe the damage threshold recorded at 10 ps and 1000 pulses a spot to be anomalous. It is higher than that at 10 ps and 100 pulses per spot and therefore does not fit with conventional damage threshold theory which states damage threshold should either plateau or decrease with an increasing number of pulses per spot. We believe this is caused by plasma occlusion reducing the laser power actually impacting the surface of the copper [48]. This effect is only relevant to this measurement due to the reduced time between pulses (increase effective repetition rate) and their longer length, meaning the plasma cloud from a previous pulse is still present upon the arrival of the next.

Based on these results a pulse length of 800 fs and 740 pulses per spot was used for all remaining experiments. This keeps the laser pulse duration firmly below the lattice response time of copper in order to minimise unwanted heating effects, and takes advantage of the damage incubation. It will also avoid the anomalous higher damage threshold seen at high numbers of pulses per spot when using 10 ps pulses.

To test the utility of DOE machining to this application we processed trenches into flat, $20 \times 10 \times 2\, mm^3$ copper samples at various working distances. To ensure final applicability we adjusted the power to optimise for a $25 - 30\, \mu m$ deep trenches. With the laser focused as presented in Fig. 1 (using the 100 mm lens for the DOE), this was found to be an average power of 6.5 W without the DOE, and 9.7 W with the DOE. This significant increase in the necessary power we believe to be partly due to the lower FPD in the beam, but also due to the greater volume of material being removed as a consequence of the beam shape, see Table 3.

Table 3. The laser processing parameters, maximum SEY and trench dimensions for each sample. Lens samples processed with a 150 mm focal length lens, DOE with a 100 mm.

Sample	DOE 1	DOE 2	DOE 3	Lens 1	Lens 2	Lens 3	Lens 4	Lens 5	Lens 6
Average Power (W)	9.7	9.7	9.7	6.5	6.5	6.5	9.7	9.7	9.7
Pulse Energy (μJ)	24.1	24.1	24.1	16.2	16.2	16.2	24.1	24.1	24.1
Focal Displacement (mm)	0	1.25	2.5	0	1.25	2.5	0	1.25	2.5
Beam Radius at Cu Surface (μm)	40.7	38.1	40.0	31.4	35.6	46.6	31.4	35.6	46.6
δ_{max}(**±0.05**)	1.0	1.2	1.1	1.2	1.5	2.2	0.9	0.9	1.3
Trench Depth (μm)	22.4	29.6	28.3	23.0	17.4	9.9	41.3	36.2	25.7
FWHM Trench Width (μm)	46.5	21.3	24.4	28.7	26.7	28.3	26.0	30.19	35.9
Aspect Ratio	0.48	1.39	1.16	0.80	0.65	0.35	1.59	1.20	0.72
Trench Area (μm^2)	815	633	666	613	444	238	1099	1027	845

We processed nine samples and characterised their SEY between a 50 eV and 1800 eV primary electron energy. The measurements were obtained by exposing the samples to electrons in an ultra-high vacuum at normal incidence and monitoring the currents from the sample and a secondary electron collector. A more thorough description of the experimental setup and

Optical Materials EXPRESS

procedure is detailed elsewhere [27,49]. The figure of merit used is δ_{max}, the maximum SEY measured across the spectrum of primary electron energies. All samples were processed with an 800 fs pulse length, a 70 μm hatch distance, 20 mm/s scan speed, and a 400 kHz repetition rate. Other parameters, trench dimensions and the δ_{max} of the samples are summarised in Table 3. while the primary electron energy dependence of the SEY are given in Fig. 5.

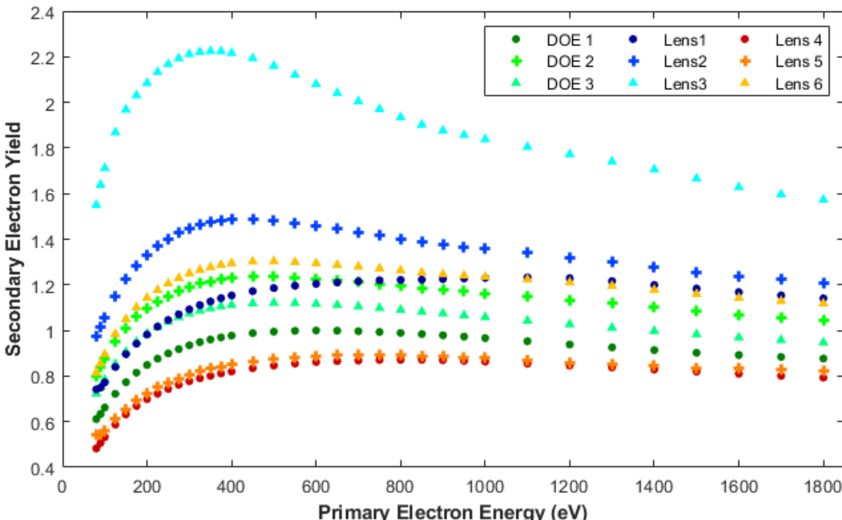

Fig. 5. SEY dependence on primary electron energy for the LESS treated copper samples. The green scale curves are those processed using the DOE and 100 mm spherical lens at 9.65 W average power, the blue are processed using only a 150 mm spherical lens at 6.49 W and the red-yellow with the 150 mm lens at 9.65 W. Circles denote processing in the focal plane, crosses 1.25 mm beyond it, and triangles 2.5 mm beyond it.

There are two key comparisons made for the treatment with and without DOE: between the trenches of same depth, and between those produced at the same power . The same depth is more relevant for our key application at the LHC where the trench depth is a more limiting factor than the laser power. Samples Lens 1-3 were made for this comparison. For other applications where the depth is not limited, we also compare at the same power in Lens 4-6.

Parameter sets DOE 1 and Lens 1 were both optimised to produce an ideal trench depth when processing in focus. Two further working distances, 1.25 mm and 2.5 mm away from the focus, were investigated at these powers to simulate processing the LHC beam screens. The same working distances were explored in the same power lens set. The SEY of each sample was measured for primary electron energies between 50 and 1800 eV. Three 2 mm^2 spots on each sample were selected randomly and an average taken in order to account for regional variation on the sample. All samples were characterised by a ZEISS Sigma 500 to obtain Field Emmission Gun Scanning Electron Microscopy using a 5 kV accelerating voltage in high current mode. Cross sections were obtained by the method outlined by Bajek *et. al.* using a Keyence VHX 7000 optical microscope [27].

First comparing at the same trench depth, DOE 1 produces a clear 'w' shaped trench profile due to the ring shape of the beam, see Fig. 6, while lens only samples have the 'u' shaped trenches seen in our previous work [27,50]. We can see that between DOE 1 and Lens 1, both processed in the focal plane, DOE 1 has a 0.24 lower SEY, despite having the same trench depth. We can see DOE 1 has a lower aspect ratio. This would normally be associated with a higher SEY, as numerically modelled by other researchers for cylindrical wells and square trenches [34,36]. However, the 'w' shape might better be modelled as two 'u' shaped trenches of a higher

aspect ratio, overlapping each other, explaining the discrepancy. Another explanation is that the wider trenches means a greater area of the surface is covered with inclined surfaces, allowing for more secondary electrons to re-enter the surface. The greater volume of material ablated and in direct contact with the laser beam also covers a larger area with nano-particles, as can be seen in Fig. 7(a). Combined these lead to a lower proportion of the surface retaining the SEY characteristics of untreated copper. Regardless of the mechanism we have shown that within our constraints the DOE provides a lower SEY with an otherwise identical optical setup, albeit while using higher power.

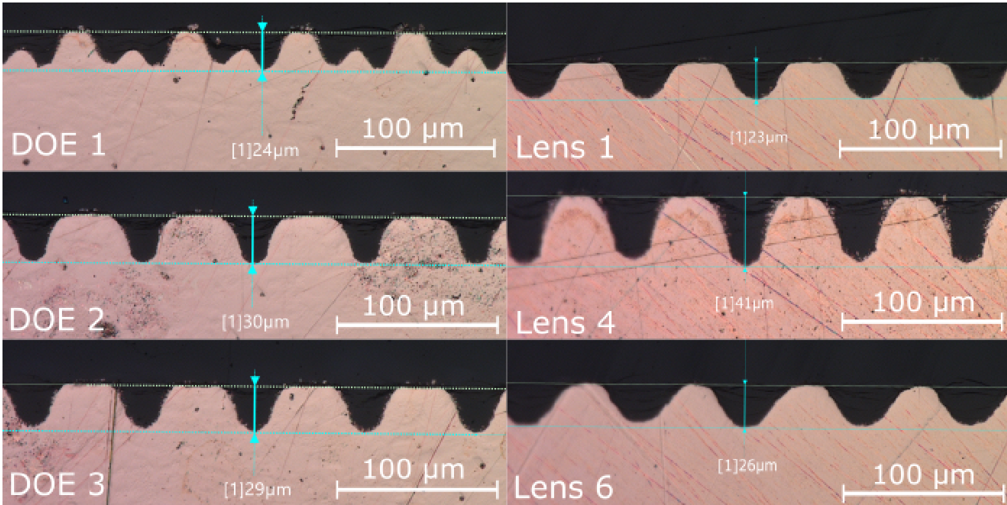

Fig. 6. Optical microscope images of cross sections from selected copper samples revealing the trench depth, width and shape.

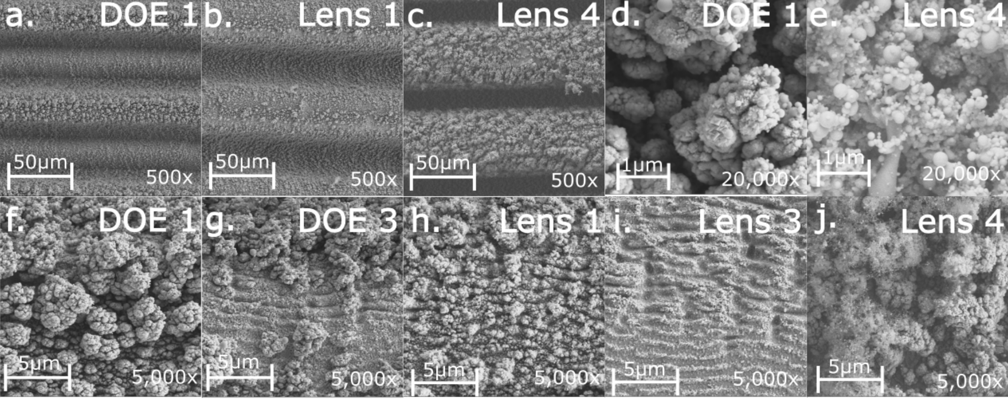

Fig. 7. SEM images of the copper samples.

As we move further out of focus, the beam produced by the DOE becomes more gaussian and this is reflected in the trench dimensions. It deepens slightly to 30 μm and reverts to the typical 'u' shape. At this working distance the SEY increased up to 1.23, just below that of Lens 1, it then drops back to 1.12 at 2.5 mm out of focus. The higher SEY of DOE 2 is consistent with our measurements of FPD, both relative and fixed, which are lower at 1.25 mm away from the focus than for DOE 1 & 3. The consistency of DOE 1-3 compared to Lens 1-3 may be attributed

Optical Materials EXPRESS

to trading off of the percentage area processed with an improved aspect ratio of the trenches as we process further out of focus. The out of focus beam shape is also producing trenches with a higher aspect ratio than the same depth trenches from a true gaussian beam (Lens 1). We find that at all working distances the SEY is below the target of 1.4 allowing it to be reduced to near unity with electron scrubbing in order to eliminate electron clouds [43,51]. This is not the case for a Gaussian beam when remaining within the depth limitations. Out of focus the SEY increases to 1.49 and then to 2.22, similar to that of untreated copper, with a 1.25 mm and 2.5 mm displacement respectively. The DOE machined trenches therefore meet the requirements for SEY reduction within the LHC. We would reasonably expect similar results in other out of focus materials processing applications, such as laser treating an uneven or curved surface [52,53].

Comparing the DOE beam to a gaussian one at the same average power, we get a lower SEY both in focus and 1.25 mm away (Lens 4 and 5) but a slightly higher one at 2.5 mm away (Lens 6). However, the trench depths for Lens 4 and 5 are deeper than the LHCs operational limits and would risk puncturing the copper layer of the beam screen leading to enlarged surface resistance at operation conditions. Ignoring this limitation, both the trench depth and the SEY vary less across working distances with the DOE. Furthermore, with the gaussian, we expect the SEY to only increase rapidly further out of the focus, as in the low power series, making alignment of the focal plane critical. This alignment is less sensitive with the DOE as we can see the fixed FPD remains higher up to 4 mm either side of the focus. This shows that for applications where an even response is needed at variable working distances, DOEs can still show significant improvement over gaussian beams when operating at the same average power and pulse energy.

Scanning electron micrographs were acquired to compare the nano-structures between the samples, selected images in Fig. 7. Micrograph a. shows a 500x image of the DOE 1 trenches. The 'w' trench shape is clearly visible as is the even nano-particle coverage. Figure 7(b). shows the 'u' shape of the Lens 1 trenches and the more sparse nano-structure coverage between the trenches. This may have been caused by the narrower radius of the beam at this working distance, meaning less of the surface was directly exposed to the laser, and could partially explain the higher SEY. They return in the higher power Lens 4 sample, Fig. 7(c). This benefits the DOE as it allows us to use higher power, obtaining the denser nano-structure, whilst maintaining the trench depth and lowering the SEY. Zooming in to 20,000x magnification we can see the detailed structure between (d.) and within (e.) the trenches. The 'cauliflowers' are less present within the trenches which have a more bubble like structure. This structure is also creating nano-trenches that should reduce the SEY.

Figure 7(f) through (j) show 5,000x magnified images of the structures in between, and at the tops the trenches. The in focus DOE, Fig. 7(f)., shows a clear covering of the 'cauliflower' structures between the trenches that we have seen in our previous work without the DOE [27]. These structures are mostly absent between the trenches in DOE 3, Fig. 7(g), revealing laser-induced periodic surface structures (LIPSS) [54–56]. These have been linked to a minor decrease in SEY but not as substantial as the nano-structure seen in f. [51]. Looking at h. we see the cauliflower structures are less dense without the DOE at the lower power. Again indicating that the higher powers are beneficial for the nano-structure as they are present in the case of Lens 4, see Fig. 7(j). At this higher power we also see a new fibrous looking structure within the trenches. This is likely also beneficial for lowering the SEY. Lens 3, see Fig. 7(i)., shows only LIPSS and no other structures, contributing to its exceptionally high SEY.

4. Conclusions

We have thoroughly investigated the optical properties of a laser beam modified by an axilens diffractive optical element. We have then shown its advantages for laser processing at a variable working distance, including a specific application to reducing the secondary electron yield of the copper, where it performed better than a conventional gaussian beam. The axilens DOE

Optical Materials EXPRESS

produces a relatively modest focal extension, however much greater extensions are commercially available. This will exacerbate the trade offs of lower FPD, greater divergence outside the focal region, and varying beam shape, but allow for more extreme out of focus processing. We have also shown an improved reduction in the SEY of copper through the use of a higher power ring shaped beam compared to a gaussian beam, despite both producing trenches of similar depth. The beam produced both notably denser nano-structure and an improved trench shape whilst removing more material, all of which contribute to the lower SEY.

Funding. Science and Technology Facilities Council (ST/T001887/1).

Disclosures. The authors declare no conflicts of interest.

Data availability. Data underlying the results presented in this paper are available in Ref. [57].

References

1. B. X. Cao, P. L. Hoang, S. Ahn, H. Kang, J. Kim, J. Noh, Z. Hao, J. Wang, P. Yao, and C. Huang, "Automatic real-time focus control system for laser processing using dynamic focusing optical system," Opt. Express **25**(23), 28427–28441 (2017).
2. D. Stadler and H.-Y. Lo, "3d laser processing with tunable lens technology," International Congress on Applications of Lasers and Electro-Optics **2016**, 1404 (2019).
3. A. Batal, A. Michalek, P. Penchev, A. Kupisiewicz, and S. Dimov, "Laser processing of freeform surfaces: A new approach based on an efficient workpiece partitioning strategy," International Journal of Machine Tools and Manufacture **156**, 103593 (2020).
4. S. Lei, X. Zhao, X. Yu, A. Hu, S. Vukelic, M. B. Jun, H. E. Joe, Y. L. Yao, and Y. C. Shin, "Ultrafast laser applications in manufacturing processes: A state-of-the-art review," Journal of Manufacturing Science and Engineering, Transactions of the ASME **142**(3), 031005 (2020).
5. L. Hazra, "Diffractive optical elements: past, present, and future," Proc. SPIE **3729**, 198–211 (1999).
6. A. V. Baez, "Fresnel zone plate for optical image formation using extreme ultraviolet and soft x radiation," J. Opt. Soc. Am. **51**(4), 405–412 (1961).
7. E. H. Anderson, D. L. Olynick, B. Harteneck, E. Veklerov, G. Denbeaux, W. Chao, A. Lucero, L. Johnson, and D. Attwood, "Nanofabrication and diffractive optics for high-resolution x-ray applications," J. Vac. Sci. Technol., B: Microelectron. Process. Phenom. **18**(6), 2970–2975 (2000).
8. C. Chang and A. Sakdinawat, "Ultra-high aspect ratio high-resolution nanofabrication for hard x-ray diffractive optics," Nat. Commun. **5**(1), 4243 (2014).
9. P. A. Hilton, D. Lloyd, and J. R. Tyrer, "Use of a diffractive optic for high power laser cutting," J. Laser Appl. **28**(1), 012014 (2015).
10. M. Kiss, N. Quack, and T. Wildi, "Diffractive optical elements in single crystal diamond," Opt. Lett. **45**(13), 3458–3461 (2020).
11. G. Račiukaitis, E. Stankevičius, P. Gečys, M. Gedvilas, C. Bischoff, E. Jäger, U. Umhofer, and F. Völklein, "Laser processing by using diffractive optical laser beam shaping technique," J. Laser Micro/Nanoeng. **6**(1), 37–43 (2011).
12. E. R. Dufresne and D. G. Grier, "Optical tweezer arrays and optical substrates created with diffractive optics," Rev. Sci. Instrum. **69**(5), 1974–1977 (1998).
13. K. Jarasiunas, R. Aleksiejunas, T. Malinauskas, V. Gudelis, T. Tamulevicius, S. Tamulevicius, A. Guobiene, A. Usikov, V. Dmitriev, and H. J. Gerritsen, "Implementation of diffractive optical element in four-wave mixing scheme for ex situ characterization of hydride vapor phase epitaxy-grown gan layers," Rev. Sci. Instrum. **78**(3), 033901 (2007).
14. S. V. Alferov, S. V. Karpeev, and S. N. Khonina, "Polarization converter for higher-order laser beams using a single binary diffractive optical element as beam splitter," Opt. Lett. **37**(12), 2385–2387 (2012).
15. E. Hecht, *Optics, 5e* (Addison-Wesley, 2002).
16. K. Uno and I. Shimizu, "Dual focus diffractive optical element with extended depth of focus," Opt. Rev. **21**(5), 668–675 (2014).
17. L. M. Sanchez-Brea, F. J. Torcal-Milla, J. D. Hoyo, A. Cuadrado, and J. A. Gomez-Pedrero, "Optimization of angular diffractive lenses with extended depth of focus," J. Opt. **22**(6), 065601 (2020).
18. F. J. T. Milla, L. M. Sanchez-Brea, and J. A. Gomez-Pedrero, "Sector-based fresnel zone plate with extended depth of focus," Optics & Laser Technology **154**, 108294 (2022).
19. B. Kaulich, D. Cojoc, E. D. Fabrizio, J. Susini, P. Facci, S. Cabrini, and T. Wilhein, "Diffractive optical elements for differential interference contrast x-ray microscopy," Opt. Express **11**(19), 2278–2288 (2003).
20. E. D. Fabrizio, D. Cojoc, V. Emiliani, S. Cabrini, M. Coppey-Moisan, E. Ferrari, V. Garbin, and M. Altissimo, "Microscopy of biological sample through advanced diffractive optics from visible to x-ray wavelength regime," Microsc. Res. Tech. **65**(4-5), 252–262 (2005).
21. G. Mikula, A. Kolodziejczyk, M. Makowski, C. Prokopowicz, and M. Sypek, "Diffractive elements for imaging with extended depth of focus," Opt. Eng. **44**(5), 058001 (2005).

22. A. Flores, M. R. Wang, and J. J. Yang, "Achromatic hybrid refractive-diffractive lens with extended depth of focus," Appl. Opt. **43**(30), 5618–5630 (2004).
23. C. Joo and S. Ryu, "Design of binary phase filters for depth-of-focus extension via binarization of axisymmetric aberrations," Opt. Express **25**(24), 30312–30326 (2017).
24. G. Tang, A. C. Hourd, and A. Abdolvand, "Nanosecond pulsed laser blackening of copper," Appl. Phys. Lett. **101**(23), 231902 (2012).
25. R. Valizadeh, O. B. Malyshev, S. Wang, S. A. Zolotovskaya, W. A. Gillespie, and A. Abdolvand, "Low secondary electron yield engineered surface for electron cloud mitigation," Appl. Phys. Lett. **105**(23), 231605 (2014).
26. R. Salemme, V. Baglin, S. Calatroni, P. Chiggiato, B. D. Girolamo, E. G.-T. Valdivieso, B. Jenninger, L. Prever-Loiri, M. Sitko, S. Wackerow, and A. Abdolvand, "First beam test of laser engineered surface structures (less) at cryogenic temperature in cern sps accelerator," J. Phys.: Conf. Ser. **1067**, 082017 (2018).
27. D. Bajek, S. Wackerow, D. A. Zanin, L. Baudin, K. Bogdanowicz, E. G.-T. Valdivieso, S. Calatroni, B. D. Girolamo, M. Sitko, M. Himmerlich, M. Taborelli, P. Chiggiato, and A. Abdolvand, "Role of surface microgeometries on electron escape probability and secondary electron yield of metal surfaces," Sci. Rep. **10**(1), 250 (2020).
28. S. Calatroni, E. G.-T. Valdivieso, A. T. P. Fontenla, M. Taborelli, H. Neupert, M. Himmerlich, P. Chiggiato, D. Bajek, S. Wackerow, and A. Abdolvand, "Optimization of the secondary electron yield of laser-structured copper surfaces at room and cryogenic temperature," Phys. Rev. Accel. Beams **23**(3), 033101 (2020).
29. G. A. Morton, H. M. Smith, and R. Wasserman, "Afterpulses in photomultipliers," IEEE Trans. Nucl. Sci. **14**(1), 443–448 (1967).
30. N. Balcon, D. Payan, M. Belhaj, T. Tondu, and V. Inguimbert, "Secondary electron emission on space materials: Evaluation of the total secondary electron yield from surface potential measurements," IEEE Trans. Plasma Sci. **40**(2), 282–290 (2012).
31. J. Yang, W. Cui, Y. Li, G. Miao, and Q. Wang, "Study on secondary electron emission of high power microwave ferrite materials," *2019 Joint International Symposium on Electromagnetic Compatibility, Sapporo and Asia-Pacific International Symposium on Electromagnetic Compatibility*, EMC Sapporo/APEMC 2019 pp. 218–221 (2019).
32. Y. Raitses, I. D. Kaganovich, A. Khrabrov, D. Sydorenko, N. J. Fisch, and A. Smolyakov, "Effect of secondary electron emission on electron cross-field current in $e \times b$ discharges," IEEE Trans. Plasma Sci. **39**(4), 995–1006 (2011).
33. G. Franchetti, I. Hofmann, W. Fischer, and F. Zimmermann, "Incoherent effect of space charge and electron cloud," Phys. Rev. ST Accel. Beams **12**(12), 124401 (2009).
34. K. Nishimura, T. Itotani, and K. Ohya, "Influence of surface roughness on secondary electron emission and electron backscattering from metal surface," Jpn. J. Appl. Phys. **33**(8R), 4727 (1994).
35. M. Pivi, F. K. King, R. E. Kirby, T. O. Raubenheimer, G. Stupakov, and F. L. Pimpec, "Sharp reduction of the secondary electron emission yield from grooved surfaces," J. Appl. Phys. **104**(10), 104904 (2008).
36. M. Ye, Y. N. He, S. G. Hu, R. Wang, T. C. Hu, J. Yang, and W. Z. Cui, "Suppression of secondary electron yield by micro-porous array structure," J. Appl. Phys. **113**(7), 074904 (2013).
37. V. Baglin, Y. Bozhko, O. Grobner, B. Henrist, N. Hilleret, C. Scheuerlein, and M. Taborelli, "The secondary electron yield of technical materials and its variation with surface treatments," in *7th European Particle Accelerator Conference (EPAC 2000)*, (2000), pp. 217–221
38. C. Swanson and I. D. Kaganovich, "Modeling of reduced secondary electron emission yield from a foam or fuzz surface," J. Appl. Phys. **123**(2), 023302 (2018).
39. J. Ludwick, A. Iqbal, D. Gortat, J. D. Cook, M. Cahay, P. Zhang, T. C. Back, S. Fairchild, M. Sparkes, and W. O'Neill, "Angular dependence of secondary electron yield from microporous gold surfaces," J. Vac. Sci. Technol., B: Nanotechnol. Microelectron.: Mater., Process., Meas., Phenom. **38**(5), 054001 (2020).
40. O. Aberle, B. Alonso, and O. Brüning, *et al.*, *High-Luminosity Large Hadron Collider (HL-LHC): Technical design report*, CERN Yellow Reports: Monographs (CERN, Geneva, 2020). https://cds.cern.ch/record/2749422.
41. Carlos Perez Dengra, "New storage and data access solution for CMS experiment in Spain towards HL-LHC era," Tech. Rep., CERN, Geneva (2022). https://cds.cern.ch/record/2803234.
42. V. Baglin, P. Lebrun, L. Tavian, and R. van Weelderen, "Cryogenic Beam Screens for High-Energy Particle Accelerators," Tech. Rep., CERN, Geneva (2013). https://cds.cern.ch/record/1507613.
43. R. Cimino, M. Commisso, T. Demma, A. G. Grilli, P. Liu, M. Pietropaoli, V. Sciarra, V. Baglin, P. Barone, and A. Bonanno, "Electron Energy Dependence of Scrubbing Efficiency to Mitigate E-cloud Formation in Accelerators," *11th European Particle Accelerator Conference* 0806233, TUPP027 (2008).
44. S. Calatroni, E. G.-T. Valdivieso, H. Neupert, V. Nistor, A. T. P. Fontenla, M. Taborelli, P. Chiggiato, O. Malyshev, R. Valizadeh, S. Wackerow, S. A. Zolotovskaya, W. A. Gillespie, and A. Abdolvand, "First accelerator test of vacuum components with laser-engineered surfaces for electron-cloud mitigation," Phys. Rev. Accel. Beams **20**(11), 113201 (2017).
45. International Organization for Standardization, "Optics and photonics – Lasers and laser-related equipment – Vocabulary and symbols," Tech. rep., International Organization for Standardization, Geneva, CH (2018), https://www.iso.org/obp/ui/#iso:std:iso:11145:ed-5:v1:en.
46. A. E. Siegman, *Lasers* (University Science Books, 1986).
47. S. Kirkwood, A. van Popta, Y. Tsui, and R. Fedosejevs, "Single and multiple shot near-infrared femtosecond laser pulse ablation thresholds of copper," Appl. Phys. A **81**(4), 729–735 (2005).

Optical Materials EXPRESS

48. L. Tunna, A. Kearns, W. O'Neill, and C. J. Sutcliffe, "Micromachining of copper using nd:yag laser radiation at 1064, 532, and 355 nm wavelengths," Optics & Laser Technology **33**(3), 135–143 (2001).
49. P. C. Pinto, S. Calatroni, H. Neupert, D. Letant-Delrieux, P. Edwards, P. Chiggiato, M. Taborelli, W. Vollenberg, C. Yin-Vallgren, J. L. Colaux, and S. Lucas, "Carbon coatings with low secondary electron yield," Vacuum **98**, 29–36 (2013).
50. M. Sitko, A. Abdolvand, and V. Baglin, *et al.*, "Towards Implementation of Laser Engineered Surface Structures for Electron Cloud Mitigation," in *Proc. 9th International Particle Accelerator Conference (IPAC'18), Vancouver, BC, Canada, April 29-May 4, 2018*, (JACoW Publishing, Geneva, Switzerland, 2018), no. 9 in International Particle Accelerator Conference, pp. 1220–1223.
51. J. J. Nivas, M. Valadan, M. Salvatore, R. Fittipaldi, M. Himmerlich, M. Rimoldi, A. Passarelli, E. Allahyari, S. L. Oscurato, A. Vecchione, C. Altucci, S. Amoruso, A. Andreone, S. Calatroni, and M. R. Masullo, "Submitter: secondary electron yield reduction by femtosecond pulse laser-induced periodic surface structuring," Surf. Interfaces **25**, 101179 (2021).
52. M. Duocastella and C. B. Arnold, "Enhanced depth of field laser processing using an ultra-high-speed axial scanner," Appl. Phys. Lett. **102**(6), 061113 (2013).
53. D. P. Hand, M. D. Fox, F. M. Haran, C. Peters, S. A. Morgan, M. A. McLean, W. M. Steen, and J. D. Jones, "Optical focus control system for laser welding and direct casting," Optics and Lasers in Engineering **34**(4-6), 415–427 (2000).
54. P. Gregorčič, M. Sedlaček, B. Podgornik, and J. Reif, "Formation of laser-induced periodic surface structures (lipss) on tool steel by multiple picosecond laser pulses of different polarizations," Appl. Surf. Sci. **387**, 698–706 (2016).
55. E. L. Gurevich, "Mechanisms of femtosecond lipss formation induced by periodic surface temperature modulation," Appl. Surf. Sci. **374**, 56–60 (2016).
56. J. Bonse, S. V. Kirner, S. Höhm, N. Epperlein, D. Spaltmann, A. Rosenfeld, and J. Krüger, "Applications of laser-induced periodic surface structures (LIPSS)," Proc. SPIE 10092, 114–122 (2017).
57. R. Uren, "Out of focus ultrafast processing of metals for reduced secondary electron yield," University of Dundee, 2023, DOE_Paper_Public_Data.zip, https://doi.org/10.15132/10000196.

128.141.192.153 {ts '2024-03-12 12:08:45'}